Testing and numerical modelling of circular CFDST cross-sections with stainless steel outer tubes in bending

Fangying Wang[a]*, Ben Young[b], Leroy Gardner[c]

[a] *Department of Civil Engineering, University of Nottingham, Nottingham, UK*
[b] *Department of Civil and Environmental Engineering, The Hong Kong Polytechnic University, Hong Kong, China.*
[c] *Department of Civil and Environmental Engineering, Imperial College London, London, UK*

*corresponding author: fangying.wang@nottingham.ac.uk

Abstract

The structural performance of circular concrete-filled double skin tubular (CFDST) cross-sections with stainless steel outer tubes has been examined herein based on experiments and numerical modelling. A laboratory testing programme comprising a total of 22 four-point bending tests was performed on seven CFDST cross-sections with varying concrete grades. The details of the test rig and procedures, as well as the key test observations, including the failure moment capacities, moment–curvature curves and failure modes, are fully reported. A numerical modelling programme was then carried out; a finite element (FE) model was first established to replicate the test observations, and then adopted to conduct a parametric study to acquire further FE data over a broader spectrum of material strengths and cross-section slendernesses. Based on the combined set of test and FE results, the general design provisions for concrete-filled carbon steel members in the current European and American design codes were evaluated for their applicability to the studied CFDST cross-sections. Overall, the results revealed that both of the examined design codes yield unduly conservative (less so for the higher concrete grades) and scattered moment resistance predictions, though some moment

resistances predicted from the European code were on the unsafe side. Modifications, including a concrete reduction factor η to reflect the reduced relative effectiveness of using higher concrete grades and a modified stress distribution considering the partial spread of plasticity, were proposed and shown to improve the consistency of the resistance predictions. Finally, the reliability of the current and modified design rules was demonstrated through statistical analyses.

Keywords: CFDST; Composite structures; Experiments; Four-point bending tests; Moment capacities; Numerical modelling; Stainless steel.

1. Introduction

Concrete-filled steel tubular (CFST) sections have been shown to offer enhanced efficiency over conventional reinforced concrete and bare steel sections for the vertical load-bearing components in heavy structural applications, such as columns in high rise buildings and piers in long-span bridges [1–4]. The improved structural performance derives principally from the composite action between the steel tube and concrete infill; in particular, the strength and ductility of the concrete infill are increased due to the confinement provided by the outer tube and the local buckling resistance of the outer tube is enhanced due to the restraining effect from the concrete infill [5]. However, with the increasing cross-section sizes needed for larger structures, the self-weight of the members grows, while the contribution of the central core area of the concrete infill to the overall flexural stiffness becomes increasingly insignificant. To address this issue, an emerging solution is to replace the inner concrete core with a hollow steel tube, thereby creating concrete-filled double skin tubular (CFDST) cross-sections [6]. This new type of concrete-filled section retains the advantages of CFST sections, while, owing to the lower self-weight, is more efficient and can offer superior performance in seismic-resisting applications [7,8]. The cost-effectiveness of the structural system can also be improved through savings in material, foundation and labour costs. CFDST cross-sectional configurations are diverse, with different combinations of outer and inner tubular profiles to suit different structural applications. CFDST cross-sections with circular outer and inner profiles (see Fig. 1), which exploit composite action to the greatest extent [9], are the focus of the present study.

Stainless steel is a high-performance construction material that provides an appealing combination of desirable mechanical and physical properties, including high strength, stiffness, and ductility, corrosion resistance and recyclability [10,11]. Use of stainless steel for the outer tubes of CFDST cross-sections has been recently proposed [12] and is expected to become more prominent in future construction to meet increasing demands on sustainability and resilience. CFDST cross-sections with outer stainless steel tubes combine the advantages of high ductility and durability that characterise stainless steel with the structural efficiency of double skin composite construction, and have clear potential for applications in aggressive and demanding environments, such as in the nuclear industry, marine and offshore engineering sectors and earthquake-prone zones.

To date, the most common application of CFDST cross-sections in practice has been for structural members in compression [6]. This has been mirrored in research, where there has been a number of experimental and numerical studies into the compressive response of CFDST members with stainless steel outer tubes subjected to axial compression, such as those on stub columns [12–17] and long columns [18,19]. In the majority of practical applications, compression members are in fact subjected to a combination of axial compression and bending, with flexure arising due to inevitable eccentricities of axial loads, frame action, second order effects and transverse loads (e.g. wind and seismic loadings) [20]. The design of such members under combined loading typically features beam-column interaction curves, for which the pure compression and pure bending resistances act as the end points. To facilitate the application of CFDST members in practice, it is of fundamental importance to advance the knowledge of the behaviour of CFDST cross-sections in bending; this has therefore become the subject of a number of recent research investigations. Experimental studies have been carried out on CFDST beams with carbon steel circular [21–24], square [22,25], rectangular [26] or dodecagonal [27] hollow sections for both the outer and inner skins; CFDST beams with different outer and inner profiles were examined in [28]. Tests on CFDST beams with slender stainless steel outer tubes have been reported by Zhao et al. [29]. Finite element (FE) modelling has also been utilised to examine the structural response of CFDST beams [23,24,27,29]. A common feature of the above studies is the conclusion that CFDST beams exhibit high ductility and enhanced moment capacity, beyond the sum of the individual parts, due to the development of composite action between the steel tubes and concrete infill; current design provisions for composite structures were also found to be rather conservative. Overall, there have been relatively few previous studies on CFDST cross-sections in bending. Further research is thus required to examine the flexural behaviour of CFDST cross-sections and to devise safe, efficient and reliable design provisions.

As part of a wider research programme initiated by the authors to explore the structural behaviour and design of CFDST members with outer stainless steel tubes [13–16], the present study focuses on circular CFDST cross-sections in bending, and features extensive testing and numerical modelling. The physical testing was conducted on seven CFDST cross-sections with three concrete grades, and comprised material testing on the metal tubes and concrete as well as 22 four-point bending tests on CFDST beam specimens. The experimental results were subsequently used for validating the FE model, based on which a parametric study was conducted considering a range of material strengths and cross-section slendernesses. The combined set of test and FE results were compared with the moment resistance predictions calculated using the general design provisions for concrete-filled carbon steel members given in EN 1994-1-1 [30] and AISC 360-16 [31], enabling the applicability of these design provisions to the studied CFDST cross-sections to be evaluated. Finally, modifications to the current design rules were proposed and verified through statistical analyses.

2. Laboratory testing

2.1 Overview

A comprehensive laboratory testing programme on the flexural response of CFDST beams with stainless steel outer tubes and high strength steel inner tubes is described. Seven CFDST cross-sections, employing Grade EN 1.4062 austenitic stainless steel CHS 165×3 (diameter × thickness in mm) and 140×3 as the outer profiles, and high strength steel hot-rolled CHS 22×4, 32×6, 38×8, 55×11 and cold-formed CHS 89×4 as the inner profiles, were examined. For each cross-section, three grades of sandwiched concrete—C40, C80 and C120—with nominal concrete cylinder compressive strengths of 40, 80 and 120 MPa, respectively, were employed. A total of 22 CFDST beam specimens, including one repeat specimen, were prepared and tested in a four-point bending configuration.

Particular attention was given to the preparation of the CFDST beam specimens. To ensure that the inner and outer tubes were located concentrically, four steel strips, with a depth of 10 mm and a thickness of 2 mm, were welded to the tubes near each end of the CFDST beams, as illustrated in Fig. 2. Together, the inner and outer tubes were milled flat at one end to achieve full contact with the flat baseplate of the concrete casting device; this ensured that concrete leakage was eliminated during the casting and curing processes.

The labelling convention of the CFDST beam specimens was designed to allow the key features of the CFDST cross-sections to be identified directly, and is explained by the following example—for specimen B-AC165×3-HC22×4-C40, the letter 'B' represents a CFDST beam specimen, the subsequent two terms, AC165×3 and HC22×4, correspond to the outer and inner tubes with the first letter referring to the tube material ('A' and 'H' denoting austenitic stainless steel and high strength steel, respectively), and the second letter 'C' indicating a CHS, followed by the nominal cross-section dimensions in mm; the last term C40 signifies the grade of the concrete infill with the nominal strength of 40 MPa. A letter 'R' is used for the repeat test. The geometric dimensions of the CFDST beam specimens, including the diameter D and thickness t of the outer and inner tubes, distinguished by subscripts 'o' and 'i'– see Fig. 1, and member length L were measured and are reported in Table 1. Material testing on the metal tubes and concrete infill of the examined CFDST sections is reported in Section 2.2, while the conduct and results of the CFDST beam testing are described in Sections 2.3 and 2.4, respectively.

2.2 Material testing and results

Tensile coupon tests were carried out to obtain the key mechanical properties and full stress–strain response of the adopted metal tubes. The material test setups, procedures and results have been fully described by the authors in Ref. [14], and are briefly summarised herein. The coupon specimens were machined longitudinally from a random location within the cross-sections of the hot-rolled tubes, and from the quarter location around the cross-sections relative to the weld position of the cold-formed tubes. The geometric dimensions of the curved coupons were generally designed in conformity with the guidance set out in ASTM E8/E8M-15a [32], but also featured two 10.5 mm diameter holes reamed at 17 mm from each end, through which steel rods were inserted to facilitate the application of tensile force to the coupons. A displacement-controlled 50 kN servo-hydraulic testing machine was employed for the purpose of testing. The acquired full stress–strain curves for the curved coupons are shown in Fig. 3, whilst the key obtained material properties, including the Young's modulus E, the static 0.2% proof and ultimate stresses $\sigma_{0.2}$ and σ_u, elongation at fracture ε_f, and Ramberg-Osgood (R-O) parameters n and m [33], are summarised in Table 2.

The material properties of the concrete infill used in the CFDST beam specimens were obtained through the testing concrete cylinders that were cast and cured alongside the corresponding beam specimens. In this study, three concrete grades—C40, C80 and C120—were prepared in the laboratory, employing the mix proportions of cement, water, fine and coarse aggregates, condensed silica fume and super plasticizer shown in Table 3. Concrete cylinder tests were carried out at 28 days after casting and on the days of the corresponding CFDST beam tests, following the testing procedures set out in ACI 318 [34].The number of cylinder tests, average measured strengths and corresponding coefficient of variation (COV) for each concrete grade is summarised in Table 4.

2.3 Four-point bending tests

A total of 22 CFDST beam specimens was tested in four-point bending to investigate their flexural behaviour and capacity under constant bending moment. A 1000 kN servo-controlled hydraulic testing machine was employed for the application of vertical loads onto the beam specimens. A repeat test was performed on a representative CFDST beam specimen B-AC165×3-HC22×4-C40R to assess the variability of the results. A photograph and a schematic diagram of the four-point bending test rig are depicted in Figs. 4(a) and 4(b), respectively. The beam specimens were simply supported between two roller supports, located 45 mm away from the specimen end sections, and loaded through a half-round and a roller at two points offset by a distance of 200 mm from the mid-span, thereby attaining central constant moment (span L_M of 400 mm—see Fig. 4(b)). The moment span was deemed to be sufficiently long to not inhibit the cross-sectional failure modes of the beams, while the shear span (i.e. the distance between the roller support and the loading point, see Fig. 4(b)) was defined to ensure that the influence of shear was small. Four profiled seatings with a length of 90 mm were used at the supports and loading points to mitigate against premature failure of the beams due to local deformation from the concentrated forces. Any possible gaps between the seatings and the specimen, arising from initial imperfections of the outer tubes, were filled using thin steel sheets. Prior to testing, the spherical bearing shown in Fig. 4 was free to adjust its position under a preload of 3 kN to achieve full contact at two loading points, after which four restraining bolts were tightened to prevent any rotation during the tests. Three 100 mm-stroke Linear Variable Displacement Transducers (LVDTs), arranged evenly along the moment span, were used to measure the vertical deflections of the specimens during testing. A displacement-controlled testing scheme with a loading rate equal to 0.2 mm/min was adopted to perform the tests. The applied loads and the readings from the LVDTs were recorded by a data logger at one-second intervals.

2.4 Test results

All the tested CFDST beams failed within the constant moment region, featuring outward local buckling of the stainless steel outer tube, cracking and crushing of the concrete infill and bending of the inner tube; a typical tested specimen, B-AC140×3-HC55×11-C80, is displayed in Fig. 5. The full range moment–curvature responses of the tested specimens are arranged by cross-section and presented in Fig. 6, where the curvature κ in the constant moment span was determined [34,35] from Eq. (1),

$$\kappa = \frac{8\left(D_M - D_L\right)}{4\left(D_M - D_L\right)^2 + L_M^2} \tag{1}$$

based on the measured vertical deflections at the mid-span and loading points (denoted as D_M and D_L, respectively). The discrepancy between the curves of the repeated tests is small, as shown in Fig. 6(a), which demonstrates the repeatability and consistency of the test results. All the moment–curvature curves of the tested CFDST beams were observed to exhibit rounded and ductile responses; this is associated with the nonlinear and ductile material stress–strain behaviour, with pronounced strain hardening, that is a characteristic of stainless steel [10]. It is also observed from the results that the increases in concrete strength within the same CFDST cross-section lead to rather limited enhancements in the moment capacity; this mirrors the findings reported in [36,37] for CFST beams.

The experimental failure moment $M_{u,test}$ and the initial flexural stiffness EI_{ini} of each CFDST beam are presented in Table 1. The flexural stiffness EI_{ini} was compared with the full flexural stiffness of the beam (prior to the occurrence of cracking or nonlinearity in the concrete), taken as $EI_{full} = E_oI_o + E_iI_i + E_cI_c$. It should be noted that the peak values of the moment were not attained for five of the 22 specimens, as marked with an asterisk in Table 1, since the moment–curvature curves were still rising despite large curvatures. For these specimens, the failure moment was defined as the bending moment at which the tangent stiffness of the moment–curvature curve at increment i, EI_i, dropped to 1% of the initial stiffness, EI_{ini}, — i.e. failure was taken at the point where EI_i/EI_{ini} = 0.01, an example of which is presented in Fig. 7. Note that, for those specimens that did reach their peak moment, the difference between the measured peak moment and the calculated moment when EI_i/EI_{ini} = 0.01 was less than 3% in all cases. Hence, for consistency, this 1% tangent stiffness definition of failure has been applied to all the specimens in the experimental and numerical programmes throughout the present study. This method was originally proposed in [39] and has been implemented to define the ultimate capacities of concrete-filled tubular members in [14–16,39]. Note that fluctuations in the recorded test data arose herein when the tangential stiffness reduced to below about 5%EI_{ini}. To address this, the determination of the point at EI_i/EI_{ini} = 0.01 was facilitate by fitting a cubic regression curve to the data for tangential stiffness ratios below 5%, as shown in Fig. 7, and defining failure as the point at which the fitted curve reached EI_i/EI_{ini} = 0.01.

3. Numerical modelling

3.1. Overview

Following the test programme, a numerical investigation was carried out utilising the finite element (FE) software ABAQUS [41], as reported in this section. The numerical modelling programme comprised a validation study, in which a FE model was established and validated with reference to the test results reported in Section 2 of this paper, and a parametric study, in which the validated FE model was employed to generate further numerical data over a broader range of material strengths and cross-section slendernesses.

3.2. Validation study

3.2.1. Development of FE model

Each of the CFDST beam test specimens presented in Section 2 of this paper was modelled based on the measured geometric dimensions using C3D8R solid elements for the concrete and S4R shell elements for the metal tubes; these element types have been widely used for the numerical simulation of concrete-filled tubular members [3,27,41–43]. Symmetry about the mid-span plane and the plane perpendicular to the axis of bending was exploited for computational efficiency—only half of the CFDST cross-section and half of the member length were modelled, with suitable boundary conditions assigned to the planes of symmetry, as shown in Fig. 8. The nodes of the stiffened area at the loading point and roller support were coupled to reference points, through which boundary conditions were applied to mimic the four-point bending configuration employed in the tests. Specifically, the reference point at the roller support (denoted R_s) was restrained against all degrees of freedom except rotation about the axis of bending and translation in the longitudinal direction of the beam, while the reference point at the loading point (denoted R_L) was restrained against all degrees of freedom other than rotation about the axis of bending and translation in both the longitudinal and vertical directions. Vertical displacements were imposed at R_L to simulate the displacement-controlled testing. Following a prior mesh sensitivity study, uniform mesh seed sizes of $\pi D_o/80$ and $\pi D_i/40$ were chosen for the outer and inner cross-sections, respectively, while the element sizes for the concrete in the CFDST cross-section were selected to be generally consistent with those of the neighbouring tubes to ensure numerical convergence. As for the mesh density in the longitudinal direction, a finer mesh was applied within the moment span where failure was expected, while a coarser mesh was adopted for the remainder of the FE model. These mesh settings were found to generate results with acceptable accuracy and computationally efficiency.

The constitutive models used in the present numerical investigation are similar to those developed in a previous numerical study conducted by the authors [14] to simulate the compressive behaviour of equivalent CFDST cross-sections. A detailed description of the constitutive models for the metal tubes and the concrete infill has been provided in [14], and only the key aspects are reported herein. For the metal tubes, the full engineering stress–strain curves, as measured from the tensile coupon tests, were defined in a piecewise linear fashion with at least 100 intervals, and introduced into ABAQUS in the form of true stress–logarithmic plastic strain. For the concrete infill, the in-built ABAQUS concrete damage plasticity (CDP) model [41] was employed. The compressive properties were characterised by a confined concrete stress–strain curve, originally proposed by Tao et al. [45] for CFST stub columns and modified by the authors [14–16] for application to CFDST stub columns with stainless steel outer tubes, while the tensile properties of the concrete were defined by a linear stress–strain curve up to $0.1f_c$, followed by a post-peak branch defined by means of fracture energy G_F, as determined from Eq. (2),

$$G_F = (0.0469 d_{\max}{}^2 - 0.5 d_{\max} + 26)\left(\frac{f_c}{10}\right)^{0.7} \tag{2}$$

where f_c is the concrete cylinder strength in MPa and d_{max} is the maximum coarse aggregate size in mm. Note that there are large regions of concrete in tension in CFDST cross-sections in bending; therefore, in some FE simulations, convergence problems triggered by concrete tensile fracture may arise and inhibit the attainment of the peak load or tracing of the post-ultimate response. In these cases, enlarged fracture energies equal to 10, 100 or 1000 times the value calculated using Eq. (2) and termed GF-10, GF-100, and GF-1000 respectively, were sequentially employed until numerical convergence was achieved, as illustrated in Fig. 9 for a typical FE model of specimen B-AC165×3-HC22×4-C40. The underlying concept is that appropriate amplification of the fracture energy delays the onset of tensile fracture in the concrete, thereby stabilising the numerical simulations; meanwhile the influence on the results is minimal, since the contribution of the concrete in tension to the overall bending resistance of CFDST cross-sections is small. This approach has been successfully used in the modelling concrete-filled tubular members in [46], and shown to achieve satisfactory results with good computational efficiency.

The interaction at the two interfaces, i.e., the outer tube-to-concrete infill and the concrete infill-to-inner tube, was mimicked by means of surface-to-surface contact in ABAQUS [41], where the normal direction at the interface was modelled by "Hard contact" and the tangential direction was simulated by adopting a Coulomb friction model, with a friction coefficient of 0.6. The same approach and friction coefficient were adopted in [14] to simulate the behaviour of equivalent CFDST cross-sections in compression. Note that shear stress limits were not specified in ABAQUS since the friction continued beyond the loss of initial bond. Residual stresses and initial local geometric imperfections were found to have no significant impact on the ultimate response of CFDST beams, primarily due to the fact that the sensitivity of the tubes to local stabilities is reduced by the support provided from the concrete infill. The inclusion of the local imperfections and residual stresses was hence considered to be unnecessary; the suitability of this assumption is supported by the successful validation against the test results in the next subsection.

3.2.2. Validation of FE model

The modified Riks method, widely adopted for solving static numerical problems with geometrical and material nonlinearities [41], was employed for the solution of all CFDST beam FE model to acquire the numerical failure moments, moment–curvature responses and failure modes. The accuracy of the developed FE model was evaluated by comparing the numerical results with the experimental observations presented in Section 2. The failure moments $M_{u,FE}$ derived from the FE model normalised by the corresponding experimentally obtained moments $M_{u,test}$ are reported in Table 1, together with the key statistical results, showing a mean value of $M_{u,FE}/M_{u,test}$ of 0.99 and a COV of 0.068. This indicates that the developed FE model yields a high degree of accuracy and consistency in predicting the experimental failure moments. Good agreement was also observed between the experimental and numerical moment–curvature curves, an example of which is displayed in Fig. 10 for a typical CFDST beam specimen, B-AC165×3-HC22×4-C40, where the initial stiffness, failure moment and general form of the experimental loading history are fully captured by the FE simulation. Excellent agreement between the test and numerical failure modes was also observed, as shown in Fig. 5. Overall, the established FE model is capable of replicating the four-point bending tests on CFDST beams, and are thus deemed to be suitable for utilisation in the parametric study.

3.3. Parametric study

Upon completion of the validation study, the developed CFDST beam FE model was used to carry out a parametric study, with the aim of expanding the test dataset over a broader range of cross-section dimensions and material strengths. The key parameters of the CFDST beam FE model are summarised in Table 5. A total of 13 cross-sections was chosen for the outer tube, with the outer diameter D_o fixed at 600 mm and the thickness t_o varied to obtain a spectrum of local slenderness D_o/t_o ranging from 10 to 200. As for the inner tube, the outer diameter D_i was kept constant at 300 mm while six different thicknesses t_i were adopted to achieve a broad range of local slenderness D_i/t_i spanning from 5 to 150. Note that the cross-section slenderness of the modelled CFDST beams, as determined by the local slenderness of the outer tube in line with the definition for CFST members, were extended beyond the current scope of EN 1994-1-1 [30] and covered both compact and non-compact sections according to the classification limits for composite sections set out in AISC 360-16 [31]. The moment spans of all the modelled CFDST beams were set equal to 1500 mm. Regarding the material strengths for the three constituent parts of the modelled CFDST beams, the measured material properties of the tested austenitic stainless steel section AC140×3 were used for the outer tubes, those of the tested high strength steel sections HC38×8, HC55×11 and HC89×4, with varying yield strengths from 433 to 1029 MPa, were adopted for the inner tubes, and three concrete strengths (C40, C80 and C120) were assigned to the concrete infill. In total, 258 numerical parametric results on CFDST beams were generated, which are employed, together with the test results reported in Section 2 and existing experimental data from Zhao et al. [29], to assess the applicability of existing provisions for the design of the studied CFDST cross-sections in the following section.

4. Discussion and assessment of design rules

4.1 General

The existing international design rules for composite structures, as set out in the European Code EN 1994-1-1 (EC4) [30] and the American Specification AISC 360-16 [31], are strictly only applicable to fully filled carbon steel tubular members. Therefore, neither of the current design codes can be directly employed for the design of CFDST members with stainless steel outer tubes. In this study, the codified design provisions in EN 1994-1-1 and AISC 360-16 for carbon steel CFST members in bending are first discussed and then assessed for their applicability to the studied CFDST beams in Sections 4.2 and 4.3. The assessment utilises the measured/modelled geometric dimensions and material properties of the test/FE specimens, with safety factors set equal to unity. Limitations on material strengths stipulated in the examined design codes are provided in Table 6, which are exceeded for some of the tested and modelled specimens; nonetheless, comparisons were still made so that possible extension of the codes beyond their current scope can be explored. Modifications to the existing design rules are proposed and presented in Section 4.4. Standard statistical analyses are subsequently performed to evaluate the reliability associated with the application of the existing and modified design rules, as reported in Section 4.5.

4.2. EN 1994-1-1 (EC4)

EN 1994-1-1 [30] allows plastic moment capacities to be utilised for circular concrete-filled steel tubular cross-sections, provided that the cross-section slenderness D_o/t_o is no greater than a maximum permitted value of $90(235/f_y)$. This limit, established largely by calibration against available test data, is more relaxed compared to the Class 2 (plastic) slenderness limit of $70(235/f_y)$ for bare steel CHS in bending [47]; this is because consideration is taken of the beneficial restraining effect of the concrete infill on ovalisation and inward local buckling of the outer tube. In the present study, the slenderness limit is modified for application to stainless steel to account for the difference in Young's modulus relative to carbon steel; the modified limit is given by $D_o/t_o \leq 90\varepsilon^2$, in which ε^2=(235/ $\sigma_{0.2,o}$)(E_o/210000). Possible relaxation of this slenderness limit is assessed in Section 4.4, following analysis of the test and FE data.

The plastic moment resistance of the studied CFDST cross-sections was calculated on the basis of a fully plastic stress distribution over the entire cross-section, by analogy with the treatment of CFST cross-sections prescribed in EN 1994-1-1 [30]. The stress distributions in the steel and concrete components are illustrated in Fig. 11(a). The stainless steel outer tube and high strength steel inner tube are capable of reaching their yield stresses $\sigma_{0.2,o}$ and $\sigma_{0.2,i}$ in both compression and tension. The contribution of the concrete infill in the tensile region is ignored as a result of concrete cracking, which is observed prior to the attainment of the failure moment capacity. As for the concrete infill in compression, due account of the confinement afforded from the outer tube is taken by allowing a concrete coefficient of 1.0, rather than the general 0.85, to be applied to the compressive concrete cylinder strength f_c. A fibre analysis approach, which has been previously adopted in the study of circular CFST members in flexure [48-51], was employed herein to determine the neutral axis position and moment resistance of the examined CFDST beams. The cross-sections were discretised into a total of 1000 horizontal fibres, as shown in Fig. 12; the thickness of each fibre was thus D_o/1000. The areas of the outer tube, inner tube and concrete infill within each fibre were determined based on the vertical position of the fibre. The position of the neutral axis (y) was set at an initial location at fibre i; the overall axial force F was then calculated by summing the axial forces in the outer and inner tubes and the concrete infill, denoted as F_o, F_i and F_c, which were obtained through integration of the corresponding stress distributions over the respective areas with reference to the assumed neutral axis location y; the neutral axis was then shifted incrementally to fibre i+1 and the process continued until the sign of F changed, implying that axial force equilibrium had been achieved and hence the true neutral axis position had been identified. Upon determination of the position of the neutral axis, the bending moment resistance predicted according to EC4 M_{EC4} was subsequently obtained for each test and FE specimen.

The applicability of the EC4 design provisions for CFST sections to the studied CFDST sections was assessed by comparing the calculated design bending moment resistances M_{EC4} with the test/FE failure moment capacities M_u. Statistical evaluations are provided in Table 7, where the mean ratios of the test/FE to the predicted failure moments M_u/M_{EC4} are equal to 1.37 and 1.17 for the CFDST cross-sections falling within and outside the cross-section slenderness limits, respectively, with the corresponding COVs equal to 0.108 and 0.140, indicating a high degree of design conservatism and scatter. This is also evident in the graphical comparisons shown in Fig. 13, where the ratios of M_u/M_{EC4} are plotted against the normalised cross-section slenderness $\lambda_{EC}=D_o/t_o\varepsilon^2$; the current EC4 limiting value of $\lambda_{EC}=90$ is also indicated. For the CFDST cross-sections falling within this limit, a general trend of increasing conservatism with decreasing λ_{EC} values can be observed. The underestimated bending resistances in the lower slenderness domain are attributed to the lack of account taken for strain hardening in the metal, particularly the stainless steel tubes [52], and the higher degree of confinement afforded by the stockier outer tubes to the concrete infill. For the CFDST cross-sections that lie beyond $\lambda_{EC}=90$, the resistance predictions remain generally conservative, but with some results on the unsafe side, indicating that these CFDST cross-sections are unable to achieve their full plastic moment capacity. This may be attributed to the occurrence of local buckling of the outer tubes prior to the development of full plasticity and the consequential reduced confinement afforded to the concrete infill. Overall, it is concluded that the EC4 design provisions yield safe-sided bending resistance predictions for CFDST cross-sections with $\lambda_{EC}<90$, but the results are somewhat scattered, indicating scope for improvement. For CFDST cross-sections with λ_{EC}>90, the resistance predictions remain generally conservative, but with an increased number on the unsafe side.

4.3. American Specification AISC 360-16

In AISC 360-16 [31], the bending moment resistance for a CFST member is dependent on the class of the cross-section. Three classes of CFST cross-sections are defined in AISC 360-16 [31], namely compact, noncompact and slender sections, on the basis of the cross-section slenderness λ, defined as D_o/t_o. The slenderness limits for compact and noncompact circular CFST sections are given by λ_p=0.09(E/f_y) and λ_r=0.31(E/f_y), respectively. The CFST compact slenderness limit λ_p is 25% higher than the corresponding limit of 0.07(E/f_y) for bare steel CHS to account for the beneficial restraining effect of the concrete infill in delaying the local buckling of the outer tube [48], while the noncompact slenderness limit λ_r is taken conservatively to be the same as that for bare steel CHS in bending. Slender CFST sections are not covered by AISC 360-16 due to a lack of experimental data and concrete placement concerns during construction [48]; λ_r is therefore also taken as the maximum permitted slenderness for CFST cross-sections in bending. In this study, λ_p and λ_r are again modified for application to stainless steel, as follows: λ_p=0.09($E_o/\sigma_{0.2,o}$) and λ_r=0.31($E_o/\sigma_{0.2,o}$), respectively.

The AISC 360-16 [31] moment resistances M_{AISC} for the studied CFDST cross-sections are determined herein with reference to the cross-section classification. Compact sections are capable of developing their full plastic moment capacity M_p, which is determined using the same approach as that given in EC4, with the only difference being that a lower concrete confinement coefficient of 0.95 is employed in AISC 360-16 [31], as shown in Fig. 11(a).

Noncompact sections cannot achieve their full plastic moment capacity due to the occurrence of local buckling in the outer tube, but are capable exceeding their elastic moment capacity M_y due to the partial spread of plasticity in the outer tube, as shown in Fig. 11 (b). The moment resistance of a noncompact cross-section is determined by linear interpolation between the plastic moment capacity M_p and the yield moment capacity M_y with respect to the cross-section slenderness λ, bound by the compact and noncompact slenderness limits of $0.09(E_o/\sigma_{0.2,o})$ and $0.31(E_o/\sigma_{0.2,o})$ respectively, as given by Eq. (3),

$$M_{AISC}=\begin{cases} M_p & \text{for compact sections} \\ M_p-\dfrac{M_p-M_y}{\left(\lambda_r-\lambda_p\right)}\left(\lambda-\lambda_p\right) & \text{for noncompact sections}\end{cases} \tag{3}$$

where M_y is determined based on first yield, assuming a linear elastic stress distribution with the maximum compressive stress limited to the yield stress $\sigma_{0.2,o}$ at the extreme compressive fibre of the outer tube and a maximum concrete compressive stress of $0.7f_c$. Note that the stress distribution in the inner tube is derived on the basis of strain compatibility, limited by first yield of the outer tube.

The accuracy of the AISC 360-16 [31] bending resistance predictions M_{AISC} was appraised with reference to the failure moment capacities M_u obtained from the experiments and numerical simulations. A graphical evaluation of the design predictions is illustrated by plotting the normalised test and FE moment capacities M_u/M_{AISC} against the normalised cross-section slenderness $\lambda_{AISC}=(D_o/t_o)(\sigma_{0.2}/E_o)$ in Fig 14, together with the compact and noncompact (and maximum) limiting slenderness values of λ_p=0.09 and λ_r=0.31. It can be seen that AISC 360-16 [31] generally yields rather conservative resistance predictions across the range of the examined cross-section slenderness values. The design predictions tend to be less conservative as the slenderness increases for the compact sections, though generally remain on the safe side; conversely, the conservatism increases, along with the scatter, with increasing slenderness for the noncompact sections. The significant conservatism and disparities are also evident from the quantitative evaluation results presented in Table 7, where the mean ratios of M_u/M_{AISC} are equal to 1.39 and 1.60, and the COVs are equal to 0.102 and 0.321, for the compact and noncompact CFDST cross-sections, respectively. In comparison with EN 1994-1-1 [30], AISC 360-16 [31] leads to more conservative moment resistance predictions for compact sections, due mainly to the lower concrete confinement coefficient, which reduces the contribution of the concrete in compression. The conservatism and scatter in the resistance predictions for noncompact sections indicates that AISC 360-16 [31] may underestimate the spread of plasticity in the metal tubes and the level of confinement afforded to the concrete in this slenderness range. Overall, the evaluation results reveal that AISC 360-16 [31] yields somewhat conservative and rather scattered moment resistance predictions when applied to CFDST cross-sections with stainless steel outer tubes.

4.4. Modifications to design rules

4.4.1 Modifications for high strength concrete

The test results showed that increasing the concrete grade from C40 to C120 only resulted in marginal increases in moment capacities for the studied CFDST beams. However, this issue is not reflected in the current design approaches in the treatment of high grade concrete; the design predictions were thus found to be less conservative with increasing concrete grades, as shown in Fig. 15. These observations have been previously made for CFST members [53] and also mirror the findings for the examined CFDST cross-sections in compression [14]. To distinguish between the effectiveness of the confinement afforded to the different concrete grades, the concrete strengths were multiplied by a reduction factor η, as given by Eq. (4), in determining the plastic moment capacities of the CFDST cross-sections studied herein.

$$\eta = \begin{cases} 1.0 - \dfrac{f_c - 50}{200} & 50 \text{ MPa} < f_c \leq 90 \text{ MPa} \\ 0.8 & f_c > 90 \text{ MPa} \end{cases} \tag{4}$$

This modification was originally proposed by Liew et al [53] for CFST members and has been implemented by the authors for CFDST cross-sections in compression [13–16]. The accuracy of the modified EC4 and AISC 360-16 capacity predictions (denoted as M_{EC4*} and M_{AISC*}) is assessed in the graphical comparisons shown in Fig. 15, revealing that more consistent and less scattered design predictions are achieved with the inclusion of η in the design calculations. This is also shown quantitatively by the reduced COV values across the range of concrete grades from C40 to C120, as reported in Table 8.

4.4.2 Modifications to bending resistance calculation

The current EC4 design approach was found to result in overpredicted moment resistances for some CFDST cross-sections that lay beyond the maximum slenderness limit of λ_{EC}=90, owing to the fact that the full plastic moment capacities could not be consistently attained for λ_{EC}>90. To address this, a modified stress distribution, considering the partial spread of plasticity over the whole section, is proposed in this study, as shown in Fig. 11(c). The stress distribution in the stainless steel outer tube is based on first yield, i.e., plastic reserves in the tension region may be utilised without any strain limit until yielding occurs at the extreme compressive fibre; hence, the resulting stress distribution is bilinear in the tension region and linear in the compression region. The stress distribution in the concrete infill features a rectangular stress block with a concrete compressive strength of 0.85f_c, with the reduced confinement coefficient of 0.85 reflecting the reduced effectiveness of the steel tube in confining the concrete due to local buckling for λ_{EC}>90.

The proposed EC4 design approach, incorporating a modified stress distribution considering the partial spread of plasticity for CFDST cross-sections beyond the current maximum slenderness limit, as well as the concrete reduction factor η for CFDST cross-sections falling within the limit, is assessed based on the results obtained from the experimental and numerical programmes. Comparisons of the modified design predictions M_{EC4*} with the test/FE results are illustrated by plotting the normalised test/FE failure moment capacities M_u/M_{EC4*} against the cross-section slenderness λ_{EC} in Fig. 16, and quantified in terms of the mean and COV values of M_u/M_{EC4*} in Table 7. It can be seen that the proposed EC4 design approach improves design consistency and significantly reduces the number of predictions on the unsafe side compared with those from the unmodified EC4 design approach. This indicates that the design proposal with the incorporation of a modified stress distribution and a concrete strength reduction factor can be applied to the design of CFDST beams across a wide range of cross-section slenderness values; the reliability of the proposals are verified by means of statistical analyses in the next subsection.

4.5. Reliability analysis and discussion

The reliability associated with the application of the current and modified EN 1994-1-1 design rules to the studied CFDST cross-sections is assessed through statistical analyses, in accordance with EN 1990 [54]. The key parameters and results from the Eurocode reliability analysis are summarised in Table 9, where $k_{d,n}$ is the design (ultimate limit state) fractile factor, b is the average ratio of the test and FE resistances to the design resistance, as defined in [55], V_δ is the COV of the tests or FE simulations relative to the resistance model, V_r is the combined COV incorporating both model and basic variable uncertainties, and γ_{M0} is the partial safety factor. As can be seen from Table 9, the required partial factors for the original and modified design rules are 0.93 and 0.92, which are less than the currently adopted value of 1.0 in EN 1994-1-1 [30], and thus both the current and modified design rules are considered to satisfy the reliability requirements of EN 1990 [54].

5. Conclusions

Laboratory testing and numerical modelling have been conducted to investigate the structural performance of circular CFDST cross-sections with stainless steel outer tubes in bending. A total of 22 four-point bending tests was performed on seven CFDST cross-sections with different concrete grades. The results obtained from the test programme, including the failure moment capacities, moment–curvature curves and failure modes, are fully reported. A numerical modelling programme was then performed to supplement the test programme. Finite element model was firstly established and validated with reference to the test results, and then adopted to perform a parametric study to obtain a numerical databank over an extended range of material strengths and cross-section slendernesses. The combined set of test and FE results was employed to assess the applicability of the general design provisions for concrete-filled carbon steel members in EN 1994-1-1 [30] and AISC-360-16 [31] to the studied CFDST cross-sections. On the basis of the graphical and quantitative assessment results, it may be concluded that (i) EN 1994-1-1 [30] results in unduly scattered and conservative moment resistance predictions, though for some cross-sections falling outside the limits of applicability specified in the code, the predictions are slightly unconservative, and (ii) AISC 360-16 [31] yields a higher degree of conservatism and scatter than EN 1994-1-1 when used to predict the moment resistance of CFDST cross-sections with stainless steel outer tubes. Modifications to the current EN 1994-1-1 [30] provisions were proposed—a concrete reduction factor η to reflect the reduced relative effectiveness of using higher concrete grades and a modified stress distribution considering the partial spread of plasticity for CFDST cross-sections beyond the current maximum slenderness limit defined in the code. The modified design rules offer improved design consistency, and the reliability was confirmed through statistical analyses in accordance with EN 1990 [54].

Acknowledgements

The authors would like to acknowledge the contribution of Dr. Cho Yong Hyun and Mr. Cheuk Him Wong for their support in the experimental programme.

References

[1] Han L-H, Li W, Bjorhovde R. Developments and advanced applications of concrete-filled steel tubular (CFST) structures: Members. Journal of Constructional Steel Research. 2014;100:211–28.

[2] Young B, Ellobody E. Experimental investigation of concrete-filled cold-formed high strength stainless steel tube columns. Journal of Constructional Steel Research. 2006;62:484–92.

[3] Qiu W, McCann F, Espinos A, Romero ML, Gardner L. Numerical analysis and design of slender concrete-filled elliptical hollow section columns and beam-columns. Engineering Structures. 2017;131:90–100.

[4] Han L-H, Hou C, Hua Y-X. Concrete-filled steel tubes subjected to axial compression: Life-cycle based performance. Journal of Constructional Steel Research. 2020;170:106063.

[5] Song Y, Li J, Chen Y. Local and post-local buckling of normal/high strength steel sections with concrete infill. Thin-Walled Structures. 2019;138:155–69.

[6] Zhao X-L, Han L-H. Double skin composite construction. Progress in Structural Engineering and Materials. 2006;8:93–102.

[7] Zhou F, Xu W. Cyclic loading tests on concrete-filled double-skin (SHS outer and CHS inner) stainless steel tubular beam-columns. Engineering Structures. 2016;127:304–18.

[8] Wang R, Han L-H, Zhao X-L, Rasmussen KJR. Analytical behavior of concrete filled double steel tubular (CFDST) members under lateral impact. Thin-Walled Structures. 2016;101:129–40.

[9] Yan X-F, Zhao Y-G. Compressive strength of axially loaded circular concrete-filled double-skin steel tubular short columns. Journal of Constructional Steel Research. 2020;170:106114.

[10] Gardner L. Stability and design of stainless steel structures – Review and outlook. Thin-Walled Structures. 2019;141:208–16.

[11] Buchanan C, Zhao O, Real E, Gardner L. Cold-formed stainless steel CHS beam-columns – Testing, simulation and design. Engineering Structures. 2020;213:110270.

[12] Han L-H, Ren Q-X, Li W. Tests on stub stainless steel–concrete–carbon steel double-skin tubular (DST) columns. Journal of Constructional Steel Research. 2011;67:437–52.

[13] Wang F, Young B, Gardner L. Experimental Study of Square and Rectangular CFDST Sections with Stainless Steel Outer Tubes under Axial Compression. Journal of Structural Engineering. 2019;145:04019139.

[14] Wang F, Young B, Gardner L. Compressive testing and numerical modelling of concrete-filled double skin CHS with austenitic stainless steel outer tubes. Thin-Walled Structures. 2019;141:345–59.

[15] Wang F, Young B, Gardner L. CFDST sections with square stainless steel outer tubes under axial compression: Experimental investigation, numerical modelling and design. Engineering Structures. 2020;207:110189.

[16] Wang F, Young B, Gardner L. Compressive behaviour and design of CFDST cross-sections with stainless steel outer tubes. Journal of Constructional Steel Research. 2020;170:105942.

[17] Wang F-C, Han L-h, Li W. Analytical behavior of CFDST stub columns with external stainless steel tubes under axial compression. Thin-Walled Structures. 2018;127:756–68.

[18] Zheng Y, He C, Zheng L. Experimental and numerical investigation of circular double-tube concrete-filled stainless steel tubular columns under cyclic loading. Thin-Walled Structures. 2018;132:151–66.

[19] Hassanein MF, Kharoob OF. Analysis of circular concrete-filled double skin tubular slender columns with external stainless steel tubes. Thin-Walled Structures. 2014;79:23–37.

[20] Gardner L, Fieber A, Macorini L. Formulae for Calculating Elastic Local Buckling Stresses of Full Structural Cross-sections. Structures. 2019;17:2–20.

[21] Uenaka K, Kitoh H, Sonoda K. Concrete filled double skin tubular members subjected to bending. Steel and Composite Structures. 2008;8:297–312.

[22] Xiong M-X, Xiong D-X, Liew JYR. Flexural performance of concrete filled tubes with high tensile steel and ultra-high strength concrete. Journal of Constructional Steel Research. 2017;132:191–202.

[23] Eom S-S, Vu Q-V, Choi J-H, Park H-H, Kim S-E. Flexural behavior of concrete-filled double skin steel tubes with a joint. Journal of Constructional Steel Research. 2019;155:260–72.

[24] Vieta VQ, Hab H, Hoanc PT. Evaluation of ultimate bending moment of circular concrete–filled double skin steel tubes using finite element analysis. Journal of Science and Technology in Civil Engineering (STCE)-NUCE. 2019;13:21–32.

[25] Zhao X-L, Grzebieta R. Strength and ductility of concrete filled double skin (SHS inner and SHS outer) tubes. Thin-walled structures. 2002;40:199–213.

[26] Tao Z, Han L-H. Behaviour of concrete-filled double skin rectangular steel tubular beam–columns. Journal of Constructional Steel Research. 2006;62:631–46.

[27] Chen J, Wang J, Xie F, Jin W-l. Behavior of thin-walled dodecagonal section double skin concrete-filled steel tubes under bending. Thin-Walled Structures. 2016;98:293–300.

[28] Han L-H, Tao Z, Huang H, Zhao X-L. Concrete-filled double skin (SHS outer and CHS inner) steel tubular beam-columns. Thin-Walled Structures. 2004;42:1329–55.

[29] Zhao H, Wang R, Lam D, Hou C-C, Zhang R. Behaviours of circular CFDST with stainless steel external tube: Slender columns and beams. Thin-Walled Structures. 2021;158:107172.

[30] EN 1994-1-1. Eurocode 4: design of composite steel and concrete structures. Part 1.1: general rules and rules for buildings. Brussels: European Committee for Standardization (CEN); 2004.

[31] AISC 360. Specification for structural steel buildings. American Institute of Steel Construction, Chicago, USA; 2016.

[32] American Society for Testing and Materials (ASTM). Standard test methods for tension testing of metallic materials. E8/E8M-15a, West Conshohocken, PA., USA: ASTM International; 2015.

[33] Gardner L, Yun X. Description of stress-strain curves for cold-formed steels. Construction and Building Materials. 2018;189:527-38.

[34] ACI 318. Building code requirements for structural concrete and commentary. Michigan, USA, Farmington Hills; 2014.

[35] Wang F, Zhao O, Young B. Flexural behaviour and strengths of press-braked S960 ultra-high strength steel channel section beams. Engineering Structures. 2019;200:109735.

[36] Deng Y-Q, Young B. Experimental Investigation of Concrete-filled High Strength Steel Square Hollow Section Members subjected to Bending. Proceedings of the 6th International Conference on Structural Engineering, Mechanics and Computation, 2016: CRC Press/Balkema.; 2016.

[37] Chen Y, Feng R, Wang L. Flexural behaviour of concrete-filled stainless steel SHS and RHS tubes. Engineering Structures. 2017;134:159–71.

[38] Chen J, Chan T-M. Experimental assessment of the flexural behaviour of concrete-filled steel tubular beams with octagonal sections. Engineering Structures. 2019;199:109604.

[39] dos Santos GB, Gardner L, Kucukler M. A method for the numerical derivation of plastic collapse loads. Thin-Walled Structures 2018;124:258–77.

[40] He A, Wang F, Zhao O. Experimental and numerical studies of concrete-filled high-chromium stainless steel tube (CFHSST) stub columns. Thin-Walled Structures. 2019;144:106273.

[41] ABAQUS. ABAQUS/standard user’s manual. Version 6.17. Dassault Systemes Simulia Corp. USA; 2017.

[42] Espinos A, Gardner L, Romero ML, Hospitaler A. Fire behaviour of concrete filled elliptical steel columns. Thin-Walled Structures. 2011;49:239-55.

[43] He A, Liang Y, Zhao O. Behaviour and residual compression resistances of circular high strength concrete-filled stainless steel tube (HCFSST) stub columns after exposure to fire. Engineering Structures. 2020;203:109897.

[44] He A, Zhao O. Experimental and numerical investigations of concrete-filled stainless steel tube stub columns under axial partial compression. Journal of Constructional Steel Research. 2019;158:405–16.

[45] Tao Z, Wang ZB, Yu Q. Finite element modelling of concrete-filled steel stub columns under axial compression. Journal of Constructional Steel Research 2013;89:121–31.

[46] Li W, Han L-H, Chan T-M. Numerical investigation on the performance of concrete-filled double-skin steel tubular members under tension. Thin-Walled Structures. 2014;79:108–18.

[47] EN 1993-1-1. Eurocode 3: design of steel structures – Part 1.1: general rules and rules for buildings. Brussels: European Committee for Standardization (CEN); 2005.

[48] Lai Z, Varma AH. Noncompact and slender circular CFT members: Experimental database, analysis, and design. Journal of Constructional Steel Research. 2015;106:220–33.

[49] Lai B, Liew JYR. Axial-moment interaction of high strength concrete encased steel composite columns: Design recommendation. Journal of Constructional Steel Research. 2020;170: 106136.

[50] Liang QQ. High strength circular concrete-filled steel tubular slender beam–columns, Part I: Numerical analysis. Journal of Constructional Steel Research. 2011;67:164-71.

[51] Patel VI, Liang QQ, Hadi MNS. Numerical simulations of circular high strength concrete-filled aluminum tubular short columns incorporating new concrete confinement model. Thin-Walled Structures. 2020;147:106492.

[52] Buchanan C, Gardner L, Liew A. The continuous strength method for the design of circular hollow sections. Journal of Constructional Steel Research. 2016;118:207-16.

[53] Liew JR, Xiong M, Xiong D. Design of concrete filled tubular beam-columns with high strength steel and concrete. Structures 2016;8;213–226.

[54] EN 1990:2002. Eurocode — Basis of structural design. European Committee for Standardization (CEN), Brussels; 2002.

[55] Meng X, Gardner L, Sadowski AJ, Rotter JM. Elasto-plastic behaviour and design of semi-compact circular hollow sections. Thin-Walled Structures. 2020;148:106486.

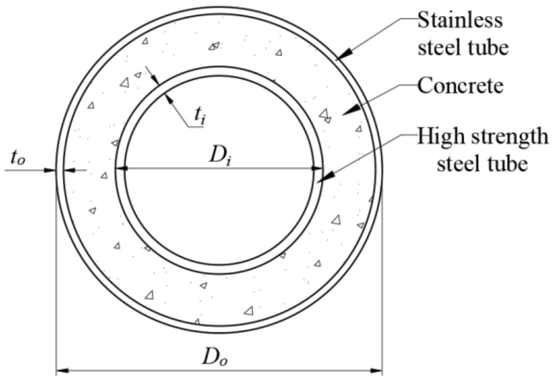

Fig. 1. Typical circular CFDST cross-section.

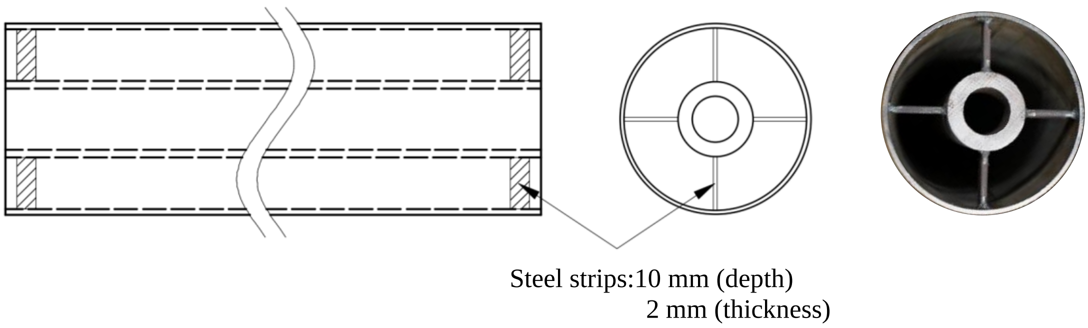

Fig. 2. Fabrication of the tubes prior to concrete casting.

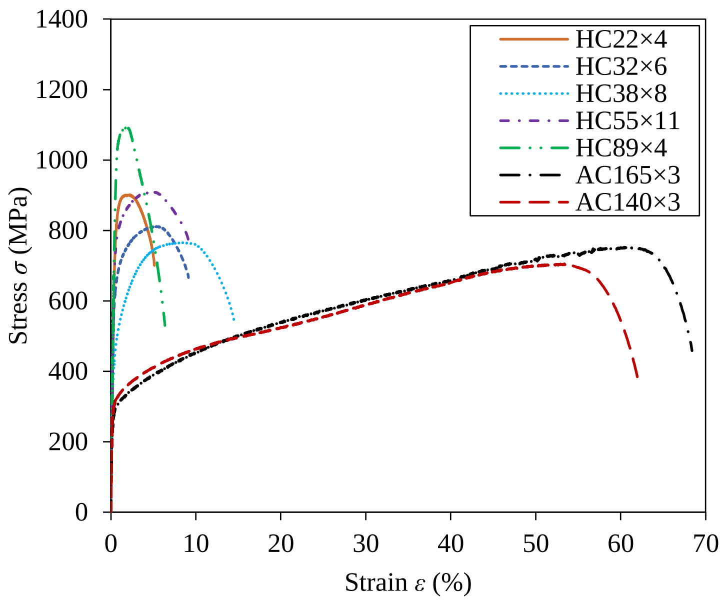

Fig. 3. Stress–strain curves measured from tensile coupon tests [14].

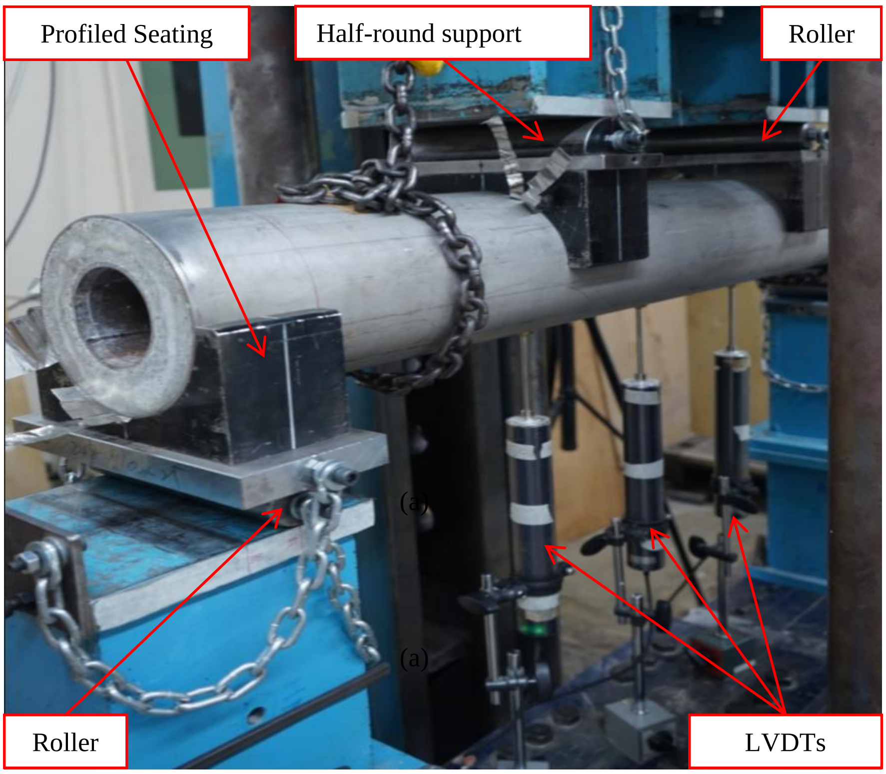

(a)

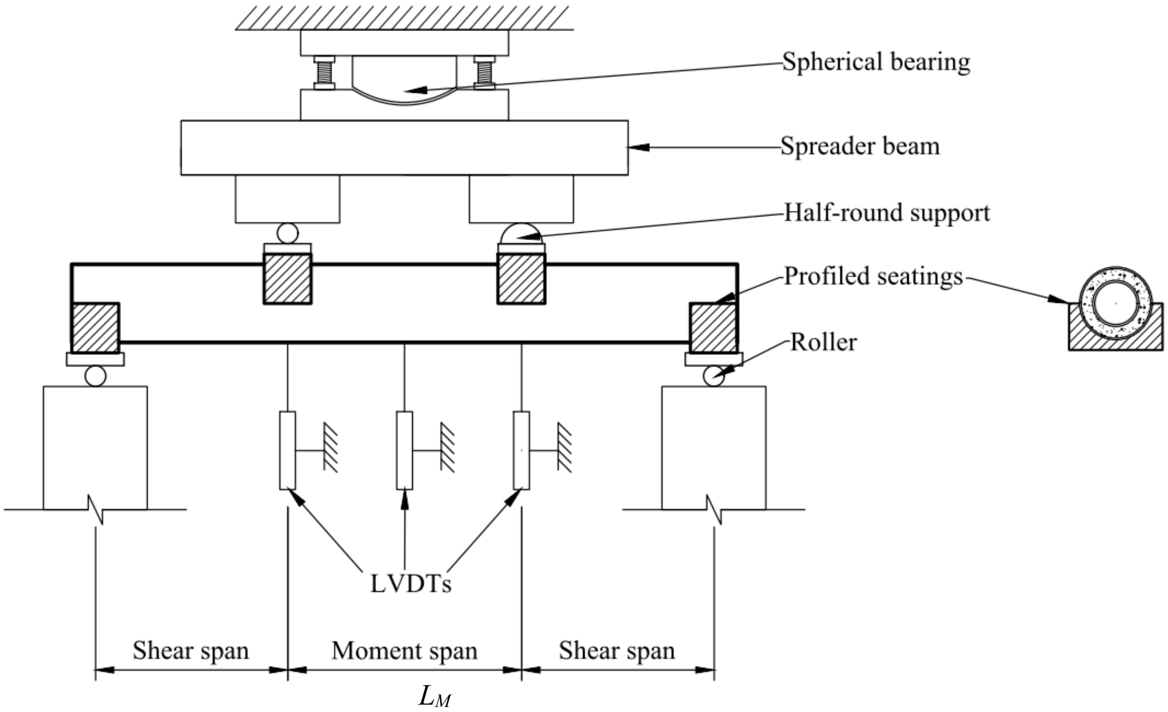

(b)

Fig. 4. Experimental setup for CFDST beam specimens: (a) Photograph (B-AC160×3-HC55×11-C80); (b) Schematic diagram.

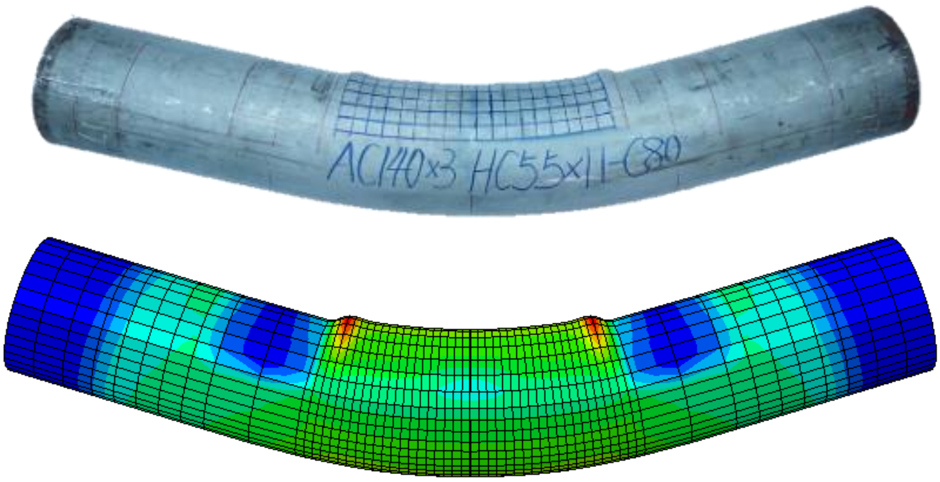

(a) Outward buckling of outer tube

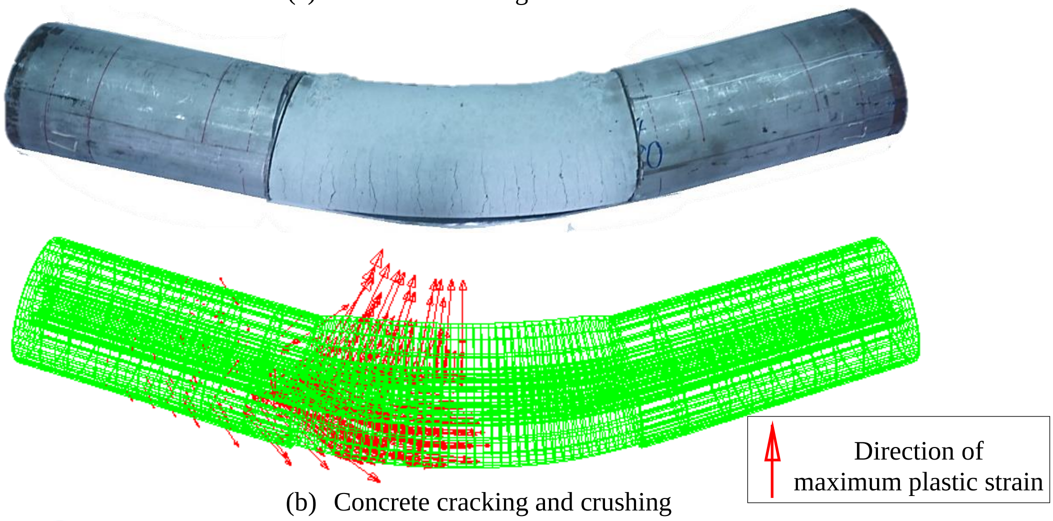

(b) Concrete cracking and crushing

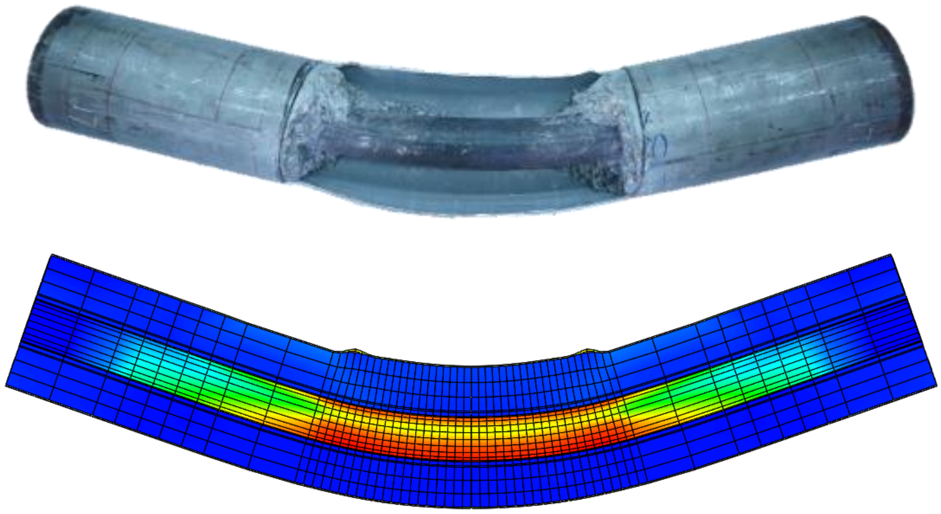

(c) Inner tube bending

Fig. 5. Test and FE failure modes of CFDST beam specimen B-AC140×3-HC55×11-C80.

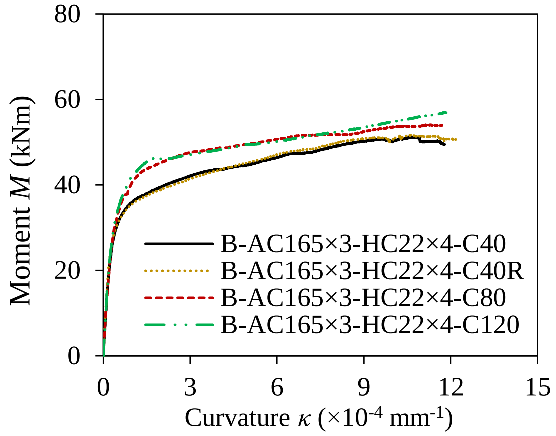

(a) AC165×3-HC22×4

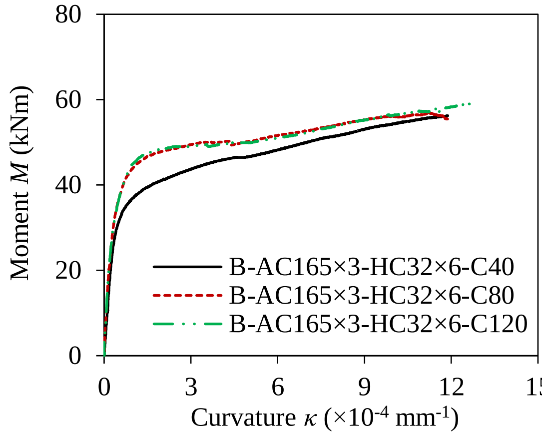

(b) AC165×3-HC32×6

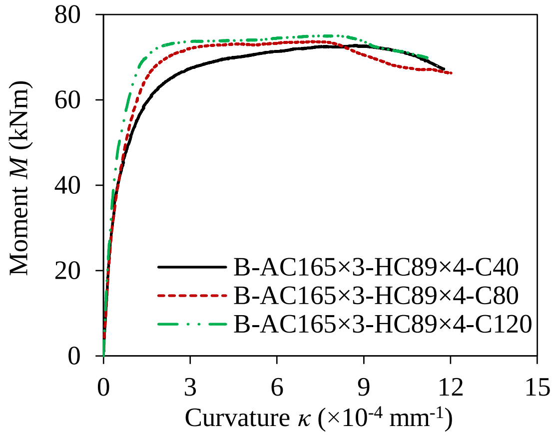

(c) AC165×3-HC89×4

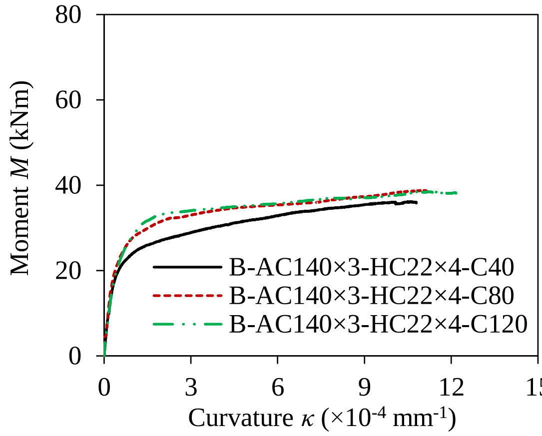

(d) AC140×3-HC22×4

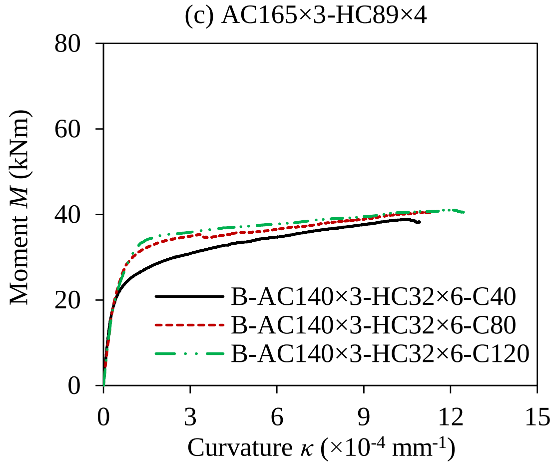

(e) AC140×3-HC32×6

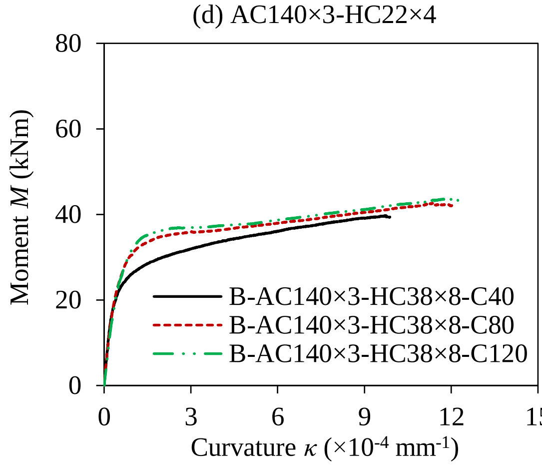

(f) AC140×3-HC38×8

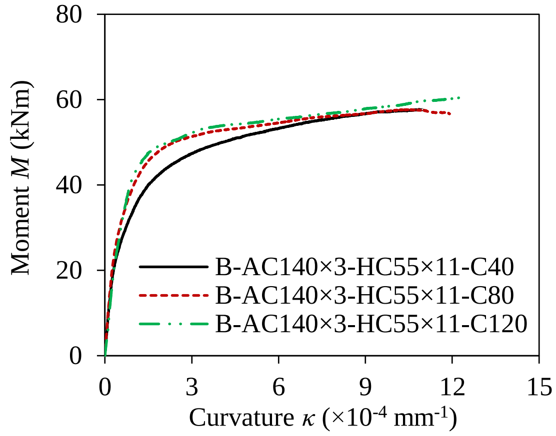

(g) AC140×3-HC55×11

Fig. 6. Moment–curvature curves of the tested CFDST beam specimens.

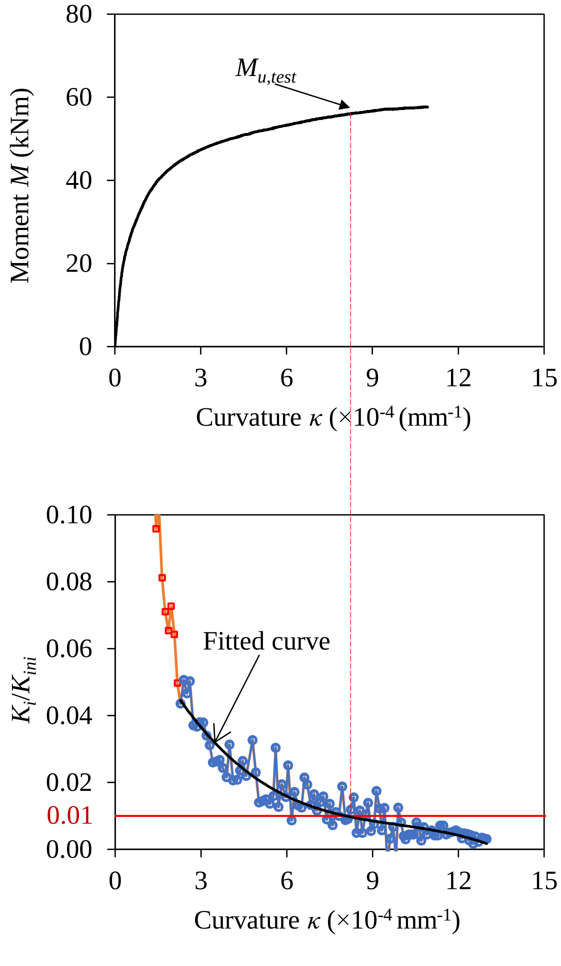

Fig. 7. Definition of experimental failure moment $M_{u,test}$ at K_i/K_{ini} = 0.01.

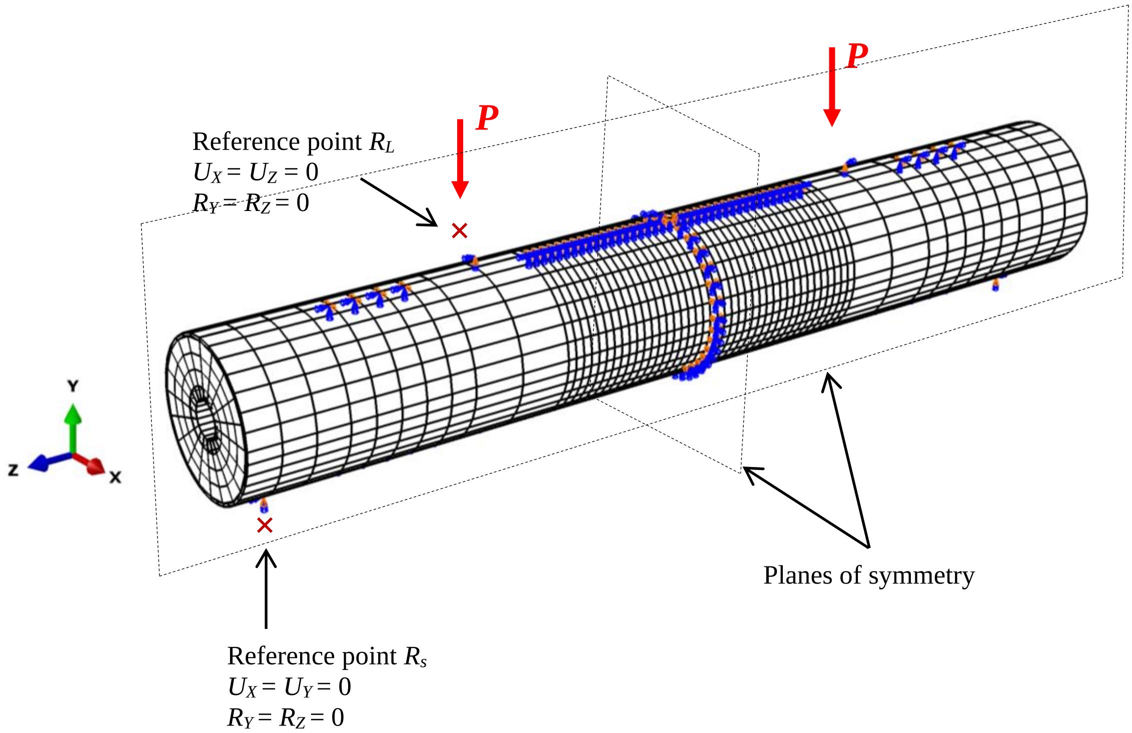

Fig. 8. CFDST beam FE model in ABAQUS.

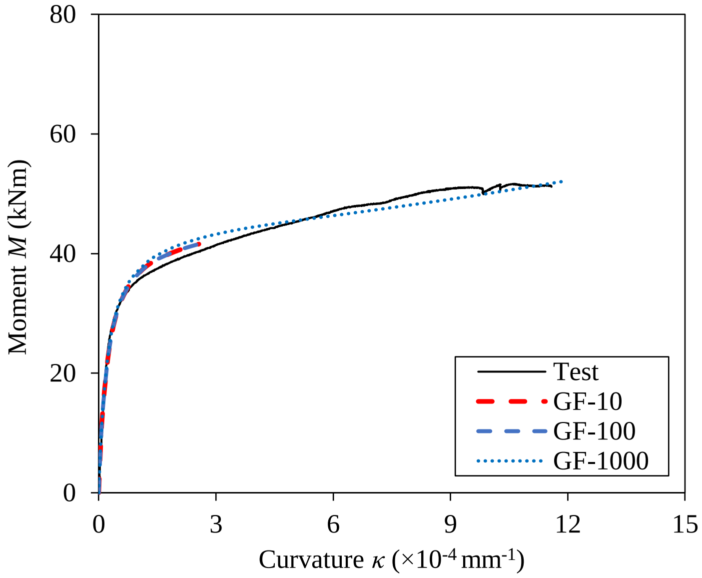

Fig. 9. Moment–curvature curves obtained from test and FE model with varying G_F values for CFDST specimen B-AC165×3-HC22×4-C40.

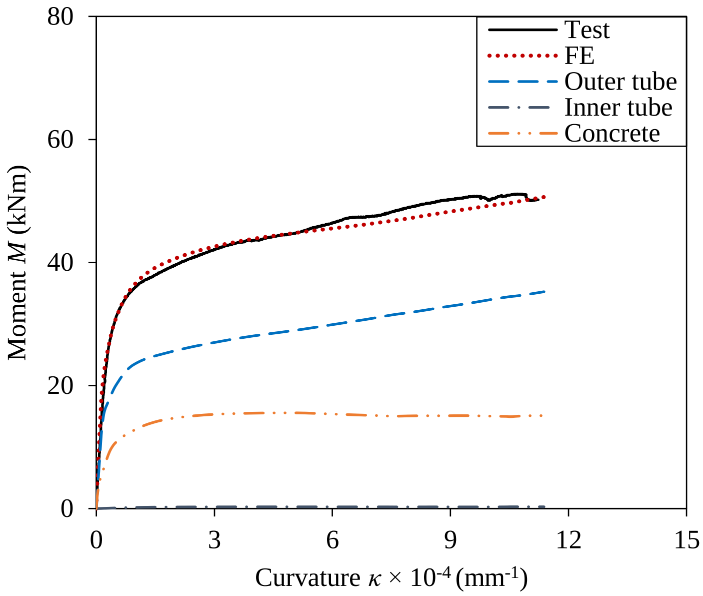

Fig. 10. Comparison of test and FE moment–curvature curves for CFDST beam specimen B-AC165×3-HC22×4-C40.

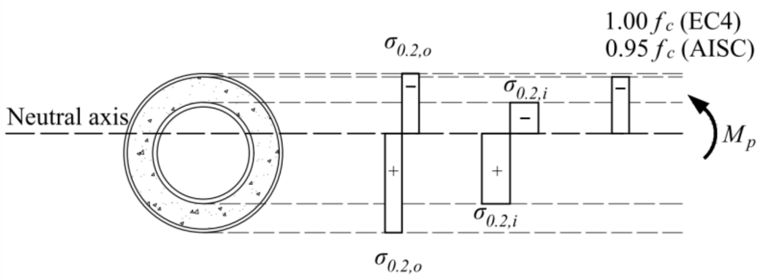

(a) Determination of M_p for compact sections in EC4 and AISC 360

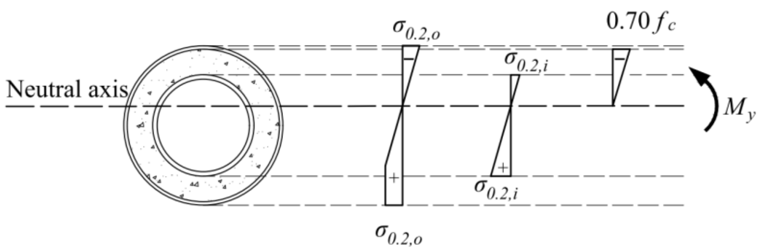

(b) Determination of M_y for noncompact sections in AISC 360

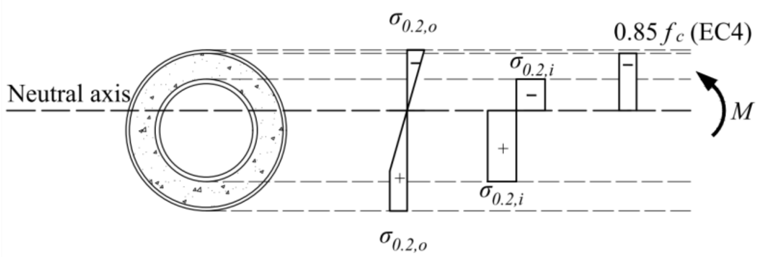

(c) Proposal for sections falling outside the slenderness limit of EC4

Fig. 11. Stress distributions for determining bending moment resistances of CFDST cross-sections.

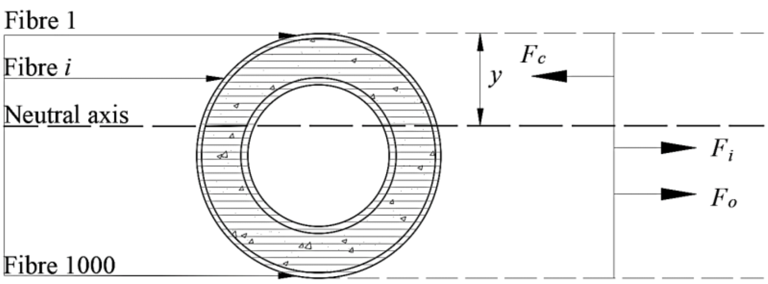

Fig. 12 Fibre analysis approach for determining the position of the neutral axis (when F_c+F_i+F_o=0) of CFDST cross-section in bending.

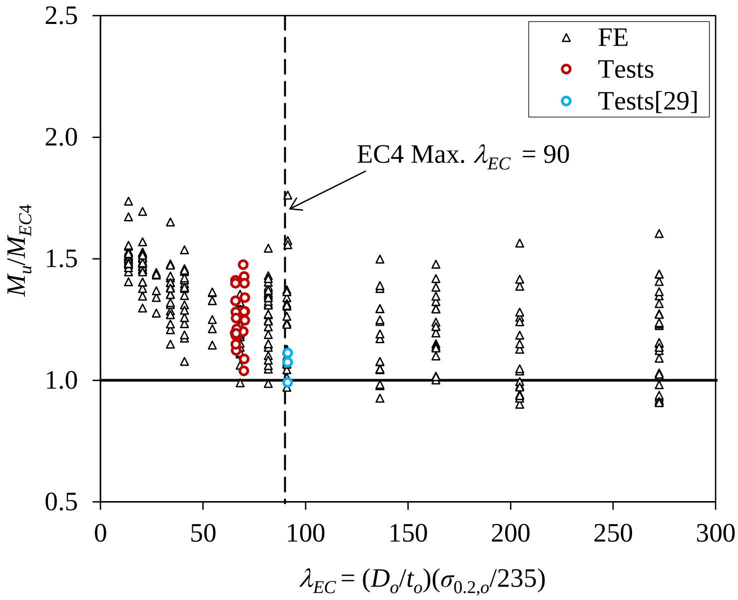

Fig. 13. Comparisons of test and FE results with moment resistance predictions from EC4.

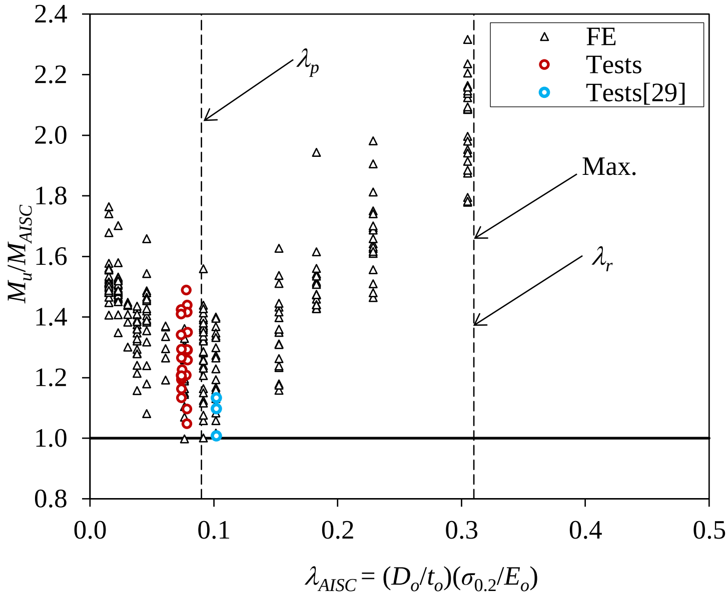

Fig. 14. Comparisons of test and FE results with moment resistance predictions from AISC 360-16.

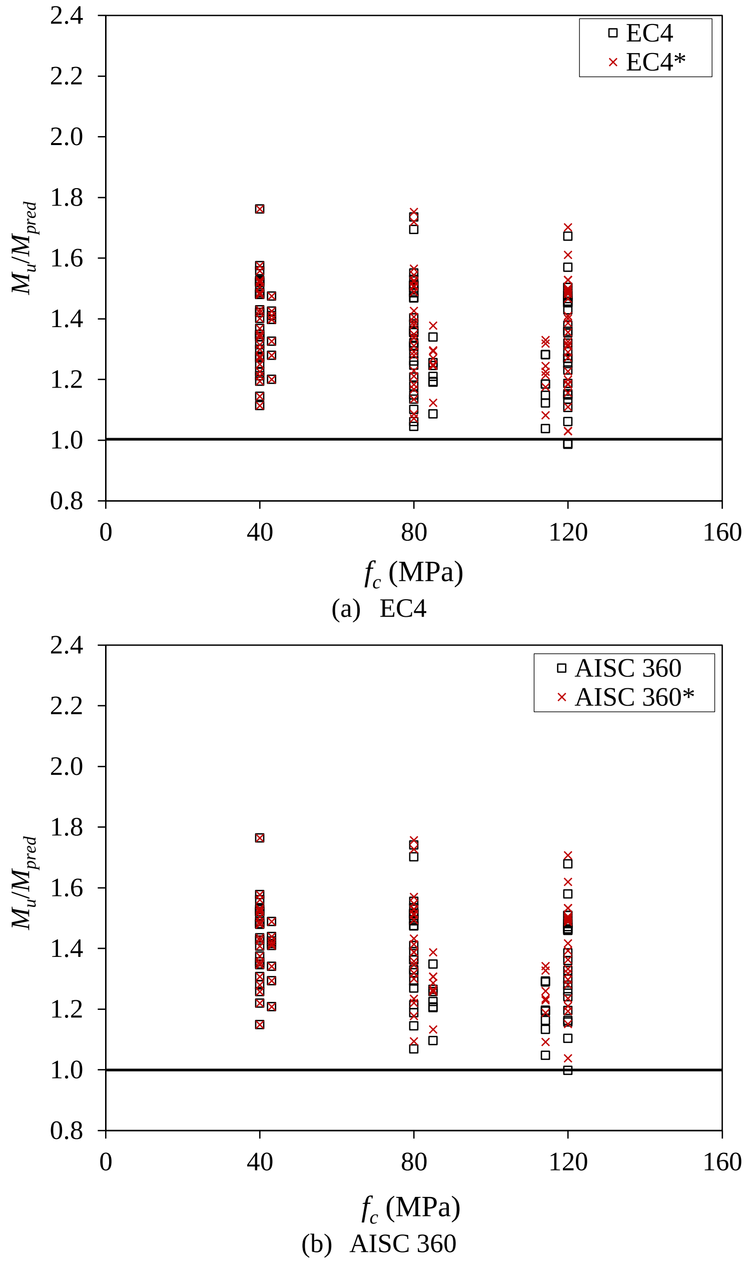

Fig. 15. Comparisons of test and FE results with current and modified moment resistance predictions from design codes.

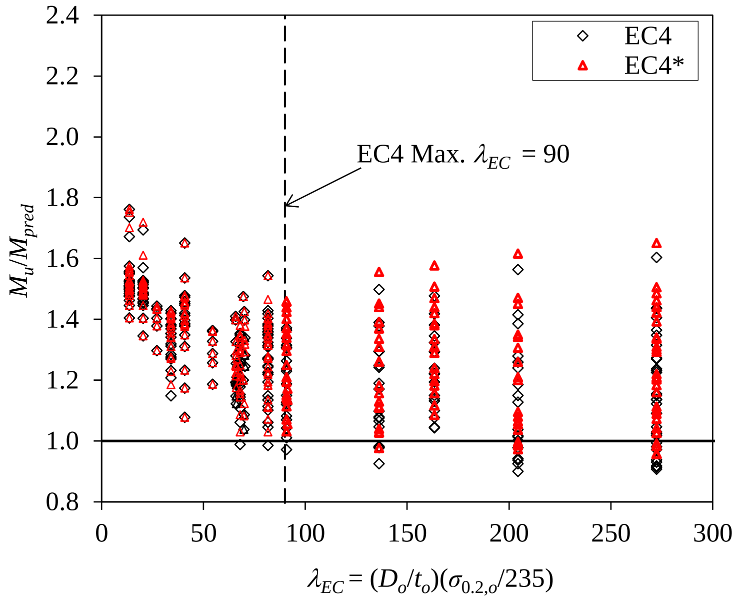

Fig. 16. Comparisons of test and FE results with moment resistance predictions from modified EC4.

Table 1. Measured geometric dimensions for CFDST beam specimens.

Specimen ID	L (mm)	D_o (mm)	t_o (mm)	D_o/t_o	D_i (mm)	t_i (mm)	D_i/t_i	$\sigma_{0.2,o}$ (MPa)	$\sigma_{0.2,i}$ (MPa)	f_c (MPa)	$M_{u,test}$ (kNm)	EI_{ini} (kNm)	EI_{ini}/EI_{full}	$M_{u,FE}/M_{u,test}$
B-AC165×3-HC22×4-C40	900	165.2	2.91	56.8	22.1	4.15	5.3	276	794	43.1	46.6	1354	0.66	0.94
B-AC165×3-HC22×4-C40R	900	165.3	2.93	56.4	22.0	4.00	5.5	276	794	43.1	48.3	1262	0.61	0.91
B-AC165×3-HC22×4-C80	900	165.3	2.90	57.0	22.0	4.05	5.4	276	794	85.0	48.7	1564	0.68	0.91
B-AC165×3-HC22×4-C120*	900	165.2	2.90	57.1	21.9	3.97	5.5	276	794	114.1	48.1	1723	0.71	1.11
B-AC165×3-HC32×6-C40*	900	165.4	2.90	57.0	31.9	5.36	6.0	276	619	43.1	48.3	1601	0.77	0.92
B-AC165×3-HC32×6-C80	900	165.3	2.90	57.0	31.9	5.61	5.7	276	619	85.0	50.2	1742	0.76	1.00
B-AC165×3-HC32×6-C120*	900	165.3	2.91	56.8	32.0	5.34	6.0	276	619	114.1	53.9	1834	0.75	1.04
B-AC165×3-HC89×4-C40	1200	165.4	2.93	56.4	89.0	3.91	22.8	276	1029	43.1	72.7	1380	0.64	0.97
B-AC165×3-HC89×4-C80	1200	165.0	2.91	56.8	88.9	3.93	22.7	276	1029	85.0	73.1	1445	0.61	0.99
B-AC165×3-HC89×4-C120	1200	165.3	2.91	56.7	89.0	3.90	22.8	276	1029	114.1	73.9	1827	0.74	1.00
B-AC140×3-HC22×4-C40	900	140.3	2.90	48.4	22.0	3.99	5.5	300	794	43.1	31.1	753	0.66	1.03
B-AC140×3-HC22×4-C80	900	140.4	2.89	48.6	21.8	3.99	5.5	300	794	85.0	34.5	800	0.64	1.02
B-AC140×3-HC22×4-C120	900	140.1	2.89	48.5	22.0	4.07	5.4	300	794	114.1	34.1	862	0.66	1.11
B-AC140×3-HC32×6-C40	900	139.9	2.89	48.4	31.9	5.23	6.1	300	619	43.1	33.6	825	0.73	0.99
B-AC140×3-HC32×6-C80	900	140.0	2.90	48.3	31.9	5.42	5.9	300	619	85.0	35.8	843	0.67	1.01
B-AC140×3-HC32×6-C120	900	140.2	2.89	48.6	32.0	5.59	5.7	300	619	114.1	36.0	904	0.69	1.10
B-AC140×3-HC38×8-C40	900	140.1	2.90	48.4	37.9	7.46	5.1	300	433	43.1	36.8	850	0.75	0.94
B-AC140×3-HC38×8-C80	900	140.2	2.87	48.8	38.0	7.63	5.0	300	433	85.0	37.1	869	0.69	0.99
B-AC140×3-HC38×8-C120	900	140.1	2.87	48.7	38.1	7.63	5.0	300	433	114.1	38.8	918	0.70	1.04
B-AC140×3-HC55×11-C40*	900	140.1	2.90	48.4	55.3	10.99	5.0	300	739	43.1	55.8	913	0.77	0.87
B-AC140×3-HC55×11-C80	900	140.2	2.88	48.6	55.1	10.72	5.1	300	739	85.0	54.0	975	0.74	0.93
B-AC140×3-HC55×11-C120*	900	140.1	2.89	48.5	55.2	10.66	5.2	300	739	114.1	55.9	1040	0.76	0.92
Mean													0.70	0.99
COV													0.074	0.068

Note: * Ultimate moment was determined as the moment where the tangent stiffness of the moment–curvature curve dropped to 1% of its initial stiffness [38].

Table 2. Measured material properties obtained from tensile coupon tests [14].

Section	$\sigma_{0.2}$ (MPa)	σ_u (MPa)	E (GPa)	ε_f (%)	n	m	$\sigma_u/\sigma_{0.2}$
AC140×3	300	705	197	62	5.3	2.5	2.35
AC165×3	276	753	200	68	4.4	2.3	2.73
HC22×4	794	901	197	5	5.8	4.1	1.14
HC32×6	619	811	208	9	5.4	3.7	1.31
HC38×8	433	765	197	15	6.2	3.0	1.77
HC55×11	739	941	211	9	8.4	3.7	1.27
HC89×4	1029	1093	209	6	5.7	4.3	1.06

Table 3. Concrete mix design [14].

Concrete grade	Mix proportions (relative to the weight of cement)					
	Cement	Water	Fine aggregate	10 mm aggregate	CSF[a]	SP[b]
C40	1.0	0.56	1.67	2.51	0.00	0.004
C80	1.0	0.32	1.25	1.88	0.00	0.020
C120	1.0	0.21	1.02	1.53	0.09	0.053

Note: [a]CSF = Condensed silica fume; [b]SP = Super plasticizer.

Table 4. Measured concrete cylinder strengths.

Concrete grade	Cylinder tests at 28 days			Cylinder tests at days of CFDST beam tests		
	No. of tests	Mean (MPa)	COV	No. of tests	Mean (MPa)	COV
C40	5	36.6	0.058	7	43.1	0.017
C80	6	76.3	0.022	6	85.0	0.032
C120	5	111.2	0.043	6	114.1	0.033

Table 5. Cross-section dimensions and material properties of CFDST beams chosen for parametric study.

$D_o \times t_o$ (mm×mm)	$\sigma_{0.2,o}$ (MPa)	$D_i \times t_i$ (mm×mm)	$\sigma_{0.2,i}$ (MPa)	f_c (MPa)
600×60, 600×40, 600×30, 600×24, 600×20, 600×15, 600×12, 600×10, 600×9, 600×6, 600×5, 600×4, 600×3	300	300×60, 300×15, 300×10, 300×5, 300×3, 300×2	433, 739, 1029	40, 80, 120

Table 6. Limitations on material strengths in design codes.

Design code	$\sigma_{0.2}$ (MPa)		f_c (MPa)	
	Min.	Max.	Min.	Max.
EN 1994-1-1	235	460	20	50
AISC 360-16	N/a	525	21	70

Table 7. Comparisons of test and FE ultimate moments with predicted moment resistances from EC4 and AISC 360-16.

Design codes	Section type	No. of results		M_u/M_{code}	
		Test	FE	Mean	COV
EC4	Falling within the EC4 limit	22	156	1.37	0.108
	Falling outside the EC4 limit	3	102	1.17	0.140
	Total	25	258	1.29	0.140
EC4*	Falling within the EC4 limit	22	156	1.38	0.102
	Falling outside the EC4 limit	3	102	1.24	0.139
	Total	25	258	1.33	0.126
AISC 360	Compact	22	126	1.39	0.102
	Noncompact	3	132	1.60	0.321
	Total	25	258	1.49	0.256

Table 8. Comparison of test and FE strengths with design predictions based on full plastic moment resistances for specimens falling within their respective codified slenderness limits.

f_c (MPa)		Ratio of test-to-predicted strengths			
		M_u/M_{EC4}	M_u/M_{EC4*}	M_u/M_{AISC}	M_u/M_{AISC*}
40	Mean	1.39	1.39	1.42	1.42
	COV	0.102	0.102	0.089	0.089
80	Mean	1.36	1.38	1.37	1.40
	COV	0.130	0.124	0.122	0.114
120	Mean	1.32	1.36	1.33	1.36
	COV	0.133	0.124	0.127	0.118
Sum	Mean	1.36	1.38	1.37	1.39
	COV	0.122	0.116	0.115	0.107

Table 9. Summary of reliability analysis results for current and modified EC4 design approaches.

Design codes	Sample type	Sample number	$k_{d,n}$	b	V_δ	γ_{M0}
EC4	Tests+FE	283	3.125	1.30	0.134	0.93
EC4*	Tests+FE	283	3.125	1.33	0.120	0.92